ADVANCED OPTICAL MATERIALS
www.advopticalmat.de

Infrared Optical Anisotropy in Quasi-1D Hexagonal Chalcogenide $BaTiSe_3$

*Boyang Zhao, Hongyan Mei, Zhengyu Du, Shantanu Singh, Tieyan Chang, Jiaheng Li, Batyr Ilyas, Qian Song, Ting-Ran Liu, Yu-Tsun Shao, Riccardo Comin, Nuh Gedik, Nicholas S. Settineri, Simon J. Teat, Yu-Sheng Chen, Stephen B. Cronin, Mikhail A. Kats, and Jayakanth Ravichandran**

Polarimetric infrared (IR) detection bolsters IR thermography by leveraging the polarization of light. Optical anisotropy, i.e., birefringence and dichroism, can be leveraged to achieve polarimetric detection. Recently, giant optical anisotropy is discovered in quasi-1D narrow-bandgap hexagonal perovskite sulfides, $A_{1+x}TiS_3$, specifically $BaTiS_3$ and $Sr_{9/8}TiS_3$. In these materials, the critical role of atomic-scale structure modulations in the unconventional electrical, optical, and thermal properties raises the broader question of the nature of other materials that belong to this family. To address this issue, for the first time, high-quality single crystals of a largely unexplored member of the $A_{1+x}TiX_3$ (X = S, Se) family, $BaTiSe_3$ are synthesized. Single-crystal X-ray diffraction determined the room-temperature structure with the *P*31*c* space group, which is a superstructure of the earlier reported $P6_3/mmc$ structure. The crystal structure of $BaTiSe_3$ features antiparallel *c*-axis displacements similar to but of lower symmetry than $BaTiS_3$, verified by the polarization dependent Raman spectroscopy. Fourier transform infrared (FTIR) spectroscopy is used to characterize the optical anisotropy of $BaTiSe_3$, whose refractive index along the ordinary ($E \perp c$) and extraordinary ($E \parallel c$) optical axes is quantitatively determined by combining ellipsometry studies with FTIR. With a giant birefringence $\Delta n \sim 0.9$, $BaTiSe_3$ emerges as a new candidate for miniaturized birefringent optics for mid-wave infrared to long-wave infrared imaging.

1. Introduction

Mid-wave infrared (MWIR) and long-wave infrared (LWIR) imaging, widely used in thermographic systems for remote sensing,[1] free-space telecommunication,[2] and surveillance,[3] utilizes the MWIR (≈3–5 µm) and LWIR (≈8–14 µm) atmospheric transmission windows,[4] to see beyond human vision. However, radiation noise, both intrinsic and from the environment,[5] limits the resolution of thermography. Polarimetric imaging relies on the polarization state of light, which changes upon the emission, scattering, or transmission of light, to improve contrast and minimize artifacts during imaging;[6] and has gained a sizable impact on military detection and recognition,[7] terrestrial monitoring and prediction,[8] and even in cosmic topology.[9]

Birefringent crystals with polarization-dependent refractive index, $\tilde{n} = n + i\kappa$, play an essential role in both the

B. Zhao, Z. Du, S. Singh, T.-R. Liu, Y.-T. Shao, J. Ravichandran
Mork Family Department of Chemical Engineering and Materials Science
University of Southern California
Los Angeles, CA 90089, USA
E-mail: j.ravichandran@usc.edu

H. Mei, M. A. Kats
Department of Electrical and Computer Engineering
University of Wisconsin–Madison
Madison, WI 53706, USA

The ORCID identification number(s) for the author(s) of this article can be found under https://doi.org/10.1002/adom.202400327

DOI: 10.1002/adom.202400327

T. Chang, Y.-S. Chen
NSF's ChemMatCARS
The University of Chicago
Lemont, IL 60439, USA

J. Li
Beijing National Laboratory for Condensed Matter Physics and Institute of Physics
Chinese Academy of Sciences
Beijing 100190, China

B. Ilyas, Q. Song, R. Comin, N. Gedik
Department of Physics
Massachusetts Institute of Technology
Cambridge, MA 02139, USA

Y.-T. Shao, J. Ravichandran
Core Center of Excellence in Nano Imaging
University of Southern California
Los Angeles, CA 90089, USA

modulation,[10,11] and detection[12,13] of light polarization. However, conventional birefringent crystals such as TiO_2,[14] $CaCO_3$,[15] $LiNbO_3$,[16] and YVO_4[17] often have appreciable absorption for MWIR and LWIR, making them insensitive to the polarization; besides, birefringent crystals designed on the asymmetric alignment of chemical bonds, ions, or molecules[18,19] commonly absorb IR as heat due to characteristic resonant IR absorptions[20] of light elements, such as H, C, O, and N. This calls for developing materials with appreciable optical anisotropy and broadband MWIR and LWIR transparency materials with appreciable optical anisotropy to control the polarization of infrared light, and highly anisotropic interband absorbers for polarized photodetection.

Hexagonal sulfides $A_{1+x}TiS_3$ (A = Ba and Sr) with quasi-one-dimensional (quasi-1D) chains of faced-shared TiS_6 octahedra[21] have giant optical anisotropy between the inter-chain (*a*-*b* plane) and intra-chain (*c*-axis) orientations.[22,23] We recently found that the optical anisotropy of crystalline $A_{1+x}TiS_3$ can originate from not only its highly anisotropic crystal structure but also subtle structural modulations[24,25] such as the *non-stoichiometric* lattice modulations[26] and the disordered TiS_6 octahedral distortions.[27] Such discoveries raise questions on the systematic differences in the structure of $A_{1+x}TiX_3$ during bandgap engineering with anion substitutions,[28,29] in the pursuit of understanding the nature of optical anisotropy and the ensuing applications. In this work, we extend the class of quasi-1D birefringent chalcogenide crystals $A_{1+x}TiX_3$ (A = Ba, Sr; X = S, Se) chalcogenides by demonstrating comparable optical anisotropy in single crystals of $BaTiSe_3$, grown for the first time. Moreover, we studied the structural similarities and distinctions with $BaTiS_3$ by carefully resolving the structure of $BaTiSe_3$ using single-crystal X-ray diffraction and Raman spectroscopy. The larger real part of the refractive index ($n_o \approx 3.2$, $n_e \approx 4.1$), compared to $BaTiS_3$ ($n_o \approx 2.61$, $n_e \approx 3.37$), has a greater birefringence of $\Delta n \approx 0.9$ in $BaTiSe_3$ and provides greater flexibility for the miniaturization of birefringent optics operating in MWIR and LWIR. The imaginary part of $BaTiSe_3$ extends the peak dichroism $\Delta\kappa$ from the ≈1.37 eV of $BaTiS_3$ to ≈1.05 eV, which makes $BaTiSe_3$ highly dichroic ($\alpha_e/\alpha_o \propto \kappa_e/\kappa_o$) till turning transparent to all polarizations below the absorption edge ≈0.20 eV, lower energy than ~0.27 eV in $BaTiS_3$.

2. $BaTiSe_3$ Crystal Growth

$BaTiSe_3$ crystals were synthesized using chemical vapor transport with iodine as the transport agent in a sealed quartz ampoule. The synthesis process is similar to that used for $BaTiS_3$,[23] and $Sr_{9/8}TiS_3$,[22] with high-purity selenide/selenium in place of sulfide/sulfur precursors (see more details in Experimental Section and Supporting Information). The synthesis temperature is held around 945 °C while an iodine transport agent maintains a steady crystal growth throughout the reaction. Aside from the predominant polycrystalline collection of $BaTiSe_3$, single crystals of $BaTiSe_3$ are found in two regions: the majority along the ampule wall (Figure S1a, Supporting Information), with rough and disordered interface between glass and $BaTiSe_3$, but of larger sizes (Figure S1e, Supporting Information); the remaining on top of or among polycrystalline $BaTiSe_3$, with cleaner surfaces (**Figure 1a**) but of smaller sizes. For simplicity in our discussion, we name the former rod-like $BaTiSe_3$ while the latter needle-like $BaTiSe_3$. Due to at least one disordered surface, we expect extended defects, i.e., domain boundaries to be present in rod-like $BaTiSe_3$. On the other hand, needle-like $BaTiSe_3$ has smoother surfaces and potentially fewer defects. Despite the sharper X-ray diffraction structure of the needle-like $BaTiSe_3$ than rod-like $BaTiSe_3$, we do not observe distinguishable optical properties between the two.

Chemical composition mapping via energy dispersion spectroscopy (EDS) attached to a scanning electron microscope (SEM) reveals uniform chemical composition across the crystal (Figure 1a), with a statistical Ba:Ti:Se atomic ratio around 20.3: 19.8: 59.9. A representative EDS spectrum and the statistical errors of the EDS analysis are shown in Figure 1b, which is close to the nominal stoichiometry of 1:1:3. Moreover, the 1:1:3 stoichiometry is also validated by the X-ray diffraction studies, which will be discussed later.

Crystal orientation is determined by out-of-plane X-ray diffraction (XRD) while varying the tilting angle (χ) about the rotational axis parallel to the long edge (Figure S2b, Supporting Information) of the needle, shown in Figure S2a (Supporting Information). Observed XRD peaks match the reported $P6_3/mmc$ structure,[30] and are indexed accordingly based on the 2θ position. The rocking curve of 020 has a full width at half maximum (FWHM) of 0.07°, showing great crystallinity of needle-like $BaTiSe_3$. Upon tilting about the long-axis of the needle-like $BaTiSe_3$, the 100-series reflections are observed around 60° tilt from each other, while 210 and 120 are observed≈30° tilt about 100 or 010. We thus confirmed the long axis of the $BaTiSe_3$ needle as the rotational axis (the *c*-axis). However, as we look closer at the off-principle-axes (not along 100, 010, or 001) reflections, the room-temperature structure of $BaTiSe_3$ reveals periodic symmetry breaking similar to the supercell modulation in $BaTiS_3$.[27,31]

3. In-Depth Crystal Structure Determination

Single-crystal X-ray diffraction (SC-XRD) resolves the crystal structure by mapping the complete X-ray diffraction structures of the reciprocal space of a single crystal up to the resolution limit.[32] SC-XRD was carried out on $BaTiSe_3$ crystals at room temperature (Table S1, Supporting Information) with high-flux X-ray synchrotron radiation at Lawrence Berkeley National Laboratory and Argonne National Laboratory. Figure 1c shows the precession maps extracted from SC-XRD of $BaTiSe_3$ along *h*0*l* and *hk*0 reciprocal planes. Although major reflections are roughly consistent with the formerly reported,[30] $P6_3/mmc$ structure,

N. S. Settineri, S. J. Teat
Lawrence Berkeley National Laboratory
Advanced Light Source
Berkeley, CA 94720, USA
N. S. Settineri
Department of Chemistry
University of California, Berkeley
Berkeley, CA 94720, USA
S. B. Cronin, J. Ravichandran
Ming Hsieh Department of Electrical Engineering
University of Southern California
Los Angeles, CA 90089, USA

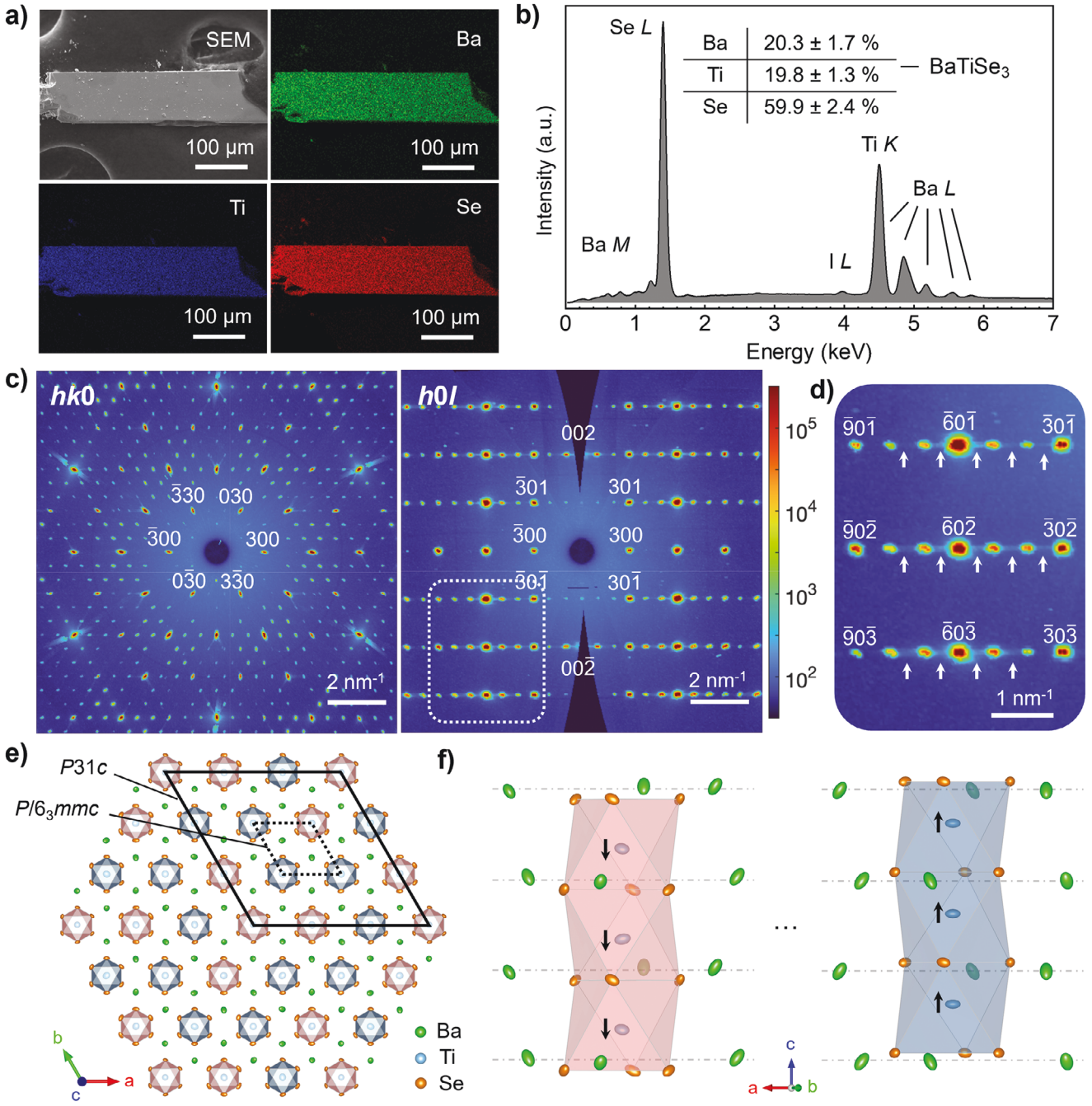

Figure 1. Characterization of $BaTiSe_3$ single crystals. a) SEM image and EDS mapping of $BaTiSe_3$ crystal. Ba, Ti, and Se are uniformly distributed across the crystal b) Quantitative chemical composition analysis of the EDS spectrum with statistical errors. The atomic ratio of Ba:Ti:Se is around 0.203:0.198:0.599, close to the theoretical 1:1:3. c) Single Crystal X-ray diffraction studies of $BaTiSe_3$ crystals show a superstructure along the *a-b* plane of the formerly reported[30] structure with $P6_3/mmc$ space group along the *a-b* plane, represented by the *hk*0 (left), and *h*0*l* or 0*kl* (right) precession reciprocal maps from single-crystal X-ray diffraction (SC-XRD). As we look closer at the intensity distribution of the observed reflections, such as the diffraction structure within the dashed box, reproduced in d), streak-like diffuse scattering is observed within the *a-b* plane (pointed out by arrows) but along the *c*-axis. Such is a sign of correlated disorders in the *a-b* plane. Nevertheless, the Bragg diffraction structure of $BaTiSe_3$ is refined as a *P*31*c* space group with a $2\sqrt{3}\times2\sqrt{3}\times1$ supercell of the $P6_3/mmc$. e) In *P*31*c*, quasi-1D chains of face-shared $TiSe_6$ octahedra are displaced along the *c*-axis in opposite directions. These chains are colored in red (downwards along the *c*-axis) and blue (upwards along the *c*-axis) whose displacement orientation is determined as in f), relative to the average Ba lattice. The *a-c* projected $TiSe_6$ chain structures of $BaTiSe_3$ in (f) also visualize the Ti atoms away from the centroid of Se_6 octahedra along the *c*-axis. This is analogous but of a different periodicity compared to $BaTiS_3$.[27]

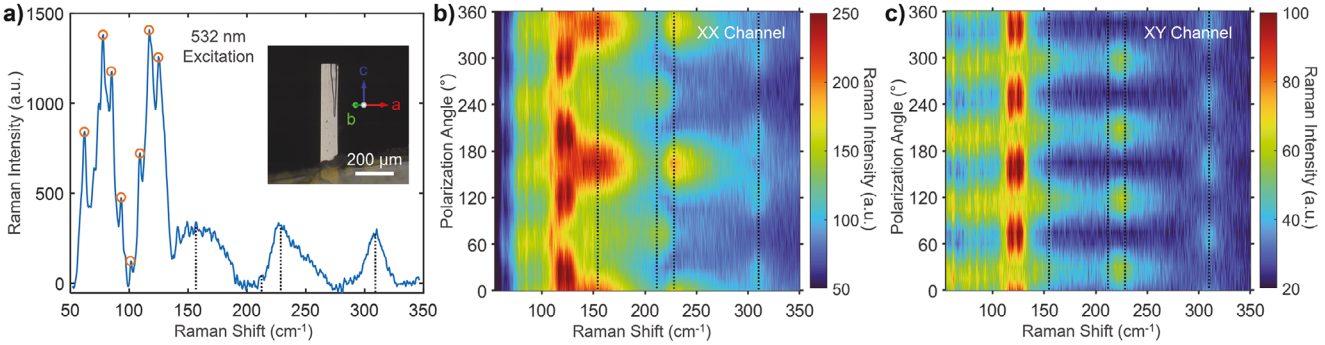

Figure 2. Room-temperature polarization dependent Raman study of $BaTiSe_3$. a) Unpolarized Raman spectrum of $BaTiSe_3$. Sharp Raman peaks (centered at 62, 77, 85, 93, 101, 109, 117, 125 cm^{-1}) are marked by orange circles, and wide Raman peaks (peaked near 152, 212, 229, 310 cm^{-1}) are marked by black dashed lines. The inset shows the optical image of the $BaTiSe_3$ crystal whose crystallographic orientation is labeled. b) Polarization-dependent Raman spectra of the XX channel, polarizations of the incident and scattered light are parallel to each other during the polarization rotation. c) Polarization-dependent Raman spectra of the XY channel, polarizations of the incident and scattered light are perpendicular to each other during the polarization rotation. The observed rotational symmetry of Raman modes is analyzed in both XX and XY channels to figure out vibrational modes, A_1, $E(x)$, and $E(y)$.

weak but symmetric satellite reflections are observed, whose periodicity matches exactly with a $2\sqrt{3} \times 2\sqrt{3} \times 1$ superstructure.

We then refine[33] $BaTiSe_3$ in 21.1 Å × 21.1 Å × 6.1 Å unit cell as a $P31c$ space group (Table S1, Supporting Information lists the refinement statistics including a refinement residual R_1 as low as 2.66%). The $P31c$ $BaTiSe_3$ breaks the translational, inversion, and mirror symmetries by adopting ordered antiparallel displaced $TiSe_6$-chains, which was also observed in the room temperature crystal structure of $BaTiS_3$.[27] Figure 1e visualizes the resulting (Tables S2 and S3, Supporting Information) supercell-ordering of the antiparallel $TiSe_6$ chain displacements, whose $P31c$ unit cell is highlighted (solid line) in comparison with $P6_3/mmc$ (dotted line). $TiSe_6$ chains are colored red (-c) and blue (+c) corresponding to the direction of chain displacement to the Ba atoms around them along the c-axis, illustrated in Figure 1f. On top of the chain displacements, Ti atoms also displace away from the centroid of $TiSe_6$ octahedra, thus leaving behind antiparallel $TiSe_6$ dipoles along the c-axis.

Moreover, strong diffuse scattering is observed between the Bragg reflections even at room temperature. Figure 1d, an $hk0$ precession reciprocal space image focusing on the dotted box in Figure 1c, highlights the streaky diffuse scattering between adjacent Bragg peaks along the a-b plane with arrows. This is analogous to the diffuse scattering in $BaTiS_3$, a sign of disordered a-b plane distortion of $TiSe_6$ octahedra which contributes to the giant optical anisotropy in $BaTiS_3$.[27] However, the magnitude of the diffuse scattering in $BaTiSe_3$ is much higher (at least 10×) than in $BaTiS_3$, making the nature of disorder a significant factor in determining the structure of $BaTiSe_3$. Hence, our current efforts in quantifying the magnitude of in-plane Ti displacements in the $TiSe_6$ octahedra between the single crystal X-ray diffraction (Figure S3, Supporting Information) and the electron diffraction (Figure S4, Supporting Information) do not agree quantitative but only qualitatively (in terms of the presence of non-negligible displacements), as discussed in the Section S5 (Supporting Information). The former technique weighs the distribution of interatomic structures across the crystal neglecting the diffuse scattering while the latter directly images the averaged structure of disorder along the [001]-zone axis of the ion-milled lamella. Therefore, further investigation into the nature of the disorder, especially how $TiSe_6$ octahedra are distorted, will be essential to understanding the $BaTiSe_3$ optical anisotropy in future works.

4. Polarization Dependent Raman Spectroscopy

The vibrational mode studies by Raman spectroscopy (**Figure 2a**) provide another perspective of the broken symmetry of $BaTiSe_3$ at a much smaller length scale (i.e., ≈1 μm). Raman spectra with parallel/perpendicular linear polarization between the incident and scattered light are shown in Figure 2b,c, as the XX and XY channels respectively. At least 12 Raman modes are observed in the background subtracted Raman spectrum in Figure 2a, each indicated with circles or dashed lines, which are far more active Raman modes[34] than $BaTiS_3$[35] under the same conditions. Considering the $P6_3/mmc$ space group $BaTiSe_3$ has only five irreducible Raman active modes,[36] (more details in Section S6, Supporting Information), $BaTiSe_3$ single crystal breaks the symmetry and forms superlattices of its reported crystal structure.[30]

To further understand the vibrational modes observed in Raman, we analyzed the active Raman modes in the space group of $P31c$ (details in Section S6, Supporting Information). Based on the observed rotational symmetries of the XX and XY channels, 117, 125, and 310 cm^{-1} are $E(x)$, 62, 77, 85, 93, 101, 109 are A_1. Wide peaks 152, 212, and 229 cm^{-1} with "dumbbell" shape two-fold rotation in the XX channel and four-fold rotation in the YY channel are hard to distinguish between A_1 and $E(y)$, but consider $E(y)$ is strongest when perpendicular to the c-axis in the XX channel, we presume 152, and 229 cm^{-1} to be $E(y)$ and 212 cm^{-1} of the opposite phase to be A_1.

5. $BaTiSe_3$ Optical Anisotropy

IR reflectance and transmittance spectra were measured by polarization-resolved Fourier transform infrared spectroscopy (FTIR). When incident light was linearly polarized parallel or

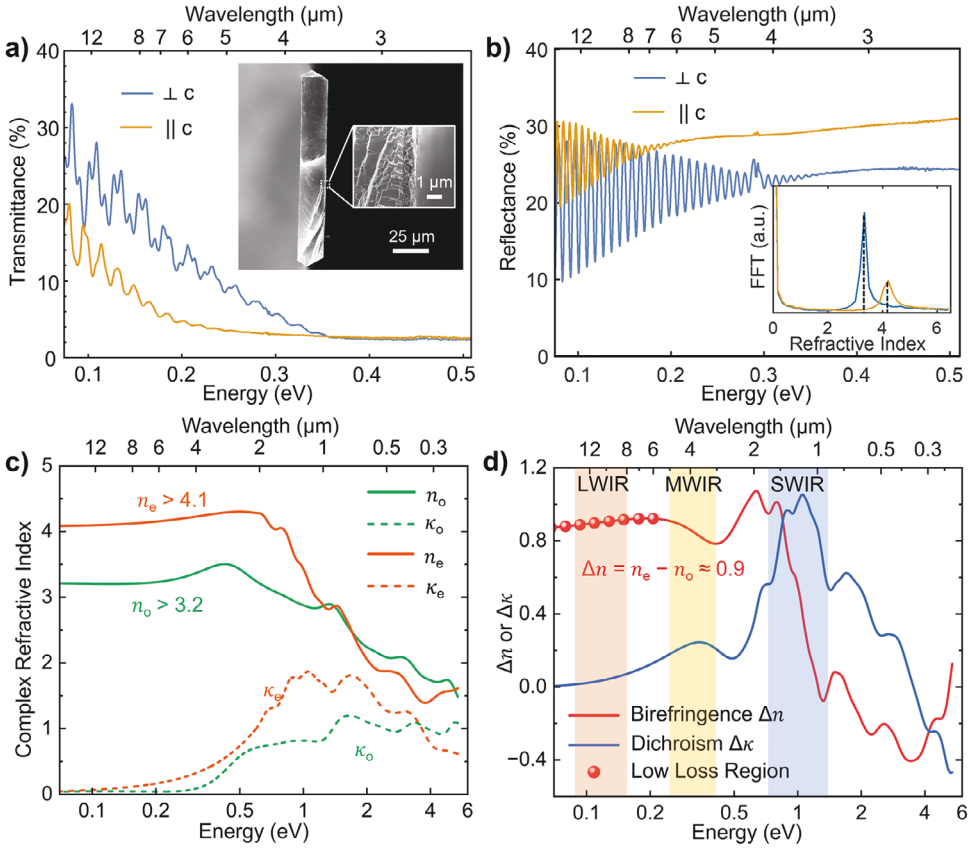

Figure 3. Optical anisotropy of $BaTiSe_3$. Polarization-resolved FTIR a) transmittance and b) reflectance spectra show large anisotropy between the ordinary (⊥ c) and the extraordinary (|| c) polarization. The absorption edge energy of the ordinary and extraordinary polarizations are observed at 0.20 and 0.33 eV, respectively, consistent with the extinction of Fabry-Perot fringes. The cross section of $BaTiSe_3$ is shown in the inset of a). The crystal thickness was measured to be 21.33 μm. Inset of b) shows FFT analysis on the reflectance spectra for the polarization-dependent refractive index of $BaTiSe_3$. c) Optical properties obtained from combining FTIR and ellipsometry, both real (n) and imaginary (κ) parts for ordinary and extraordinary linear polarizations. d) The large dichroism ($\Delta\kappa = \kappa_o - \kappa_e$) peak across SWIR leaves behind a giant birefringence ($\Delta n = n_e - n_o$) up to 0.9 across the MWIR to LWIR wavelengths.

perpendicular to the uniaxial optical axis, which is the c-axis based on the trigonal $P31c$ crystal structure, anisotropic transmittance (**Figure** 3a) and reflectance (Figure 3b) spectra were observed. The limited thickness uniformity, as shown in the inset of Figure 3a, and the crystal tilting perturbs the Fabry-Perot fringes in the transmittance spectra and leads to appreciable scattering. Nevertheless, the anisotropic absorption edges of the extraordinary (|| c) and ordinary (⊥ c) optical polarization were clear and extracted to be 0.20 and 0.33 eV. Further, the Fabry-Perot fringes of the reflectance spectra (Figure 3b), measured on the smooth front surface, show extinction at the energies consistent with the absorption edges seen in the transmission spectra (Figure 3a).

As the refractive index is relatively constant within the transparent regime, the Fabry–Pérot interference between the top and bottom surfaces of $BaTiSe_3$ has a free spectral range of:[37]

$$\Delta\nu \approx \frac{c}{2nl\cos\theta} = \frac{c}{2l\cos\theta} \cdot \frac{1}{n} \quad (1)$$

where ν is the frequency, c is the vacuum velocity of light, n is the real part of the refractive index, l is the crystal thickness ≈21.33 μm, and θ is the incident angle. We thus carry out a fast Fourier transform (FFT) for the Fabry–Pérot fringes on the reflectance spectrum on the significantly smoother top surface (Figure 3b) to approximate the spectrum-averaged real part of the refractive index (n)[38] between the 0.075 and 0.2 eV. The inset of Figure 3b shows the resultant FFT spectrum of refractive index, with a birefringence of $n_e - n_o \approx 0.9$.

To fully quantify the degree of optical anisotropy, we then combined variable-angle ellipsometry measurements over the spectral range of 210 to 2500 nm with the polarization-resolved reflection and transmission measurements over 1.5 to 17 μm and quantitatively extracted the complex refractive index of $BaTiSe_3$ for wavelengths from 210 nm (5.9 eV) to 17 μm (0.073 eV) in Figure 3c. The details of the dielectric function extraction and the corresponding fitting parameters are discussed in Section S7 (Supporting Information) along with Figures S6–S8 (Supporting Information) and Table S4 (Supporting Information), a methodology consistent with the dielectric function extraction of $BaTiS_3$,[21] and $Sr_{1.125}TiS_3$.[26] The resulting birefringence ($\Delta n = n_e - n_o$) and dichroism ($\Delta\kappa = \kappa_o - \kappa_e$) are then plotted in Figure 3d. The dichroism becomes largest near 1 eV, within the short-wave infrared (SWIR) spectrum range, and the birefringence is as large as 0.9 across MWIR and LWIR. As the low-loss

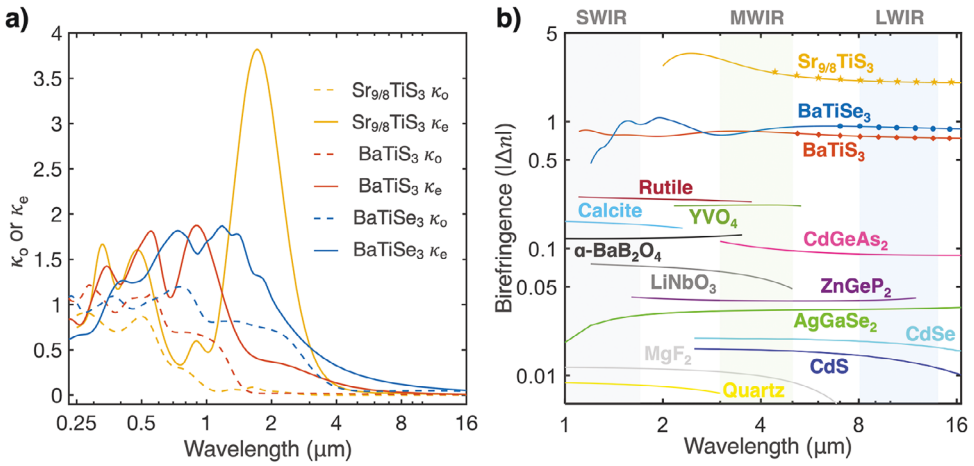

Figure 4. Comparison of the refractive index of $A_{1+x}TiX_3$ (A = Sr, Ba; X = S, Se). a) Extinction coefficients, κ_o and κ_e, of $Sr_{9/8}TiS_3$, $BaTiS_3$, and $BaTiSe_3$. b) The absolute birefringence value of a variety of IR birefringent crystals (from the literature,[14–17,21,26,39–43]) quasi-1D perovskite chalcogenides $Sr_{9/8}TiS_3$, $BaTiS_3$, and $BaTiSe_3$ extends the largest birefringence to ≈0.7 – 2.1. The symbols indicate low-loss regions of $BaTiSe_3$, $BaTiS_3$, and $Sr_{9/8}TiS_3$.

regime of $BaTiSe_3$ occurs below 0.20 eV, red spheres marked its spectrum range in Figure 3d.

First-principles calculations (for details see Experimental Section and Figures S9–S11, Supporting Information) were carried out on the *P*31*c*-$BaTiSe_3$, without considering the disordered *a*-*b* plane Ti displacements. Figure S10 (Supporting Information) compares the experimental and calculated birefringence of $BaTiSe_3$. Since *P*31*c* represents only the ordered structural characteristics of $BaTiSe_3$, the calculated birefringence mismatch between the calculated and experimental magnitude and trend of the birefringence spectrum, especially below 0.5 eV, might originate from the disordered distortion of the $TiSe_6$ octahedra like $BaTiS_3$.[27] We then speculate the anomalous but more complicated $BaTiSe_3$ *a*-*b* plane Ti displacements are one of the factors toward the birefringence of $BaTiSe_3$, the proof of such assumption should require further investigation of the disordering nature of $BaTiSe_3$.

We, therefore, compare the optical anisotropy of $A_{1+x}TiX_3$ (A = Sr, Ba; X = S, Se). The imaginary part of the refractive index (or extinction coefficient), κ_o and κ_e, of $BaTiS_3$,[21] $BaTiSe_3$, and $Sr_{9/8}TiS_3$,[26] are compared with each other in **Figure 4a**. Contrary to the κ peak featuring a sharp drop of absorption that decays to ≈0 near 4 μm in in $Sr_{1+x}TiS_3$, $BaTiS_3$ and $BaTiSe_3$ have κ peaks at shorter wavelengths but decay gradually to zero until ≈5 and ≈6 μm. Such absorption characteristic of $BaTiS_3$ and $BaTiSe_3$ leads to dichroism of a broader spectrum range but also cause more loss (reflectance + transmittance < 100%) in the LWIR region compared to $Sr_{9/8}TiS_3$. Although not comparable to the magnitude of dichroism in $Sr_{1.125}TiS_3$, $BaTiSe_3$ has comparable dichroism at longer wavelengths than $BaTiS_3$, extending the spectrum ranges of the polarization-dependent photodetection.[12]

The room temperature birefringence (Δn) and the low loss regions (after the absorption edge) of $BaTiS_3$,[21] $BaTiSe_3$, and $Sr_{9/8}TiS_3$,[26] are then listed for wavelengths from 1 to 17 μm in Figure 4, along with a variety of IR birefringent crystals.[14–17,39–43] $BaTiS_3$ and $BaTiSe_3$ share similar structural features, especially the existence of the ordered displacements along the *c*-axis and the disordered *a*-*b* plane Ti displacements, and comparable birefringence. The birefringence of $BaTiSe_3$ (Δn = ~0.9) slightly surpasses the birefringence of $BaTiS_3$ (Δn = ~0.76). $Sr_{9/8}TiS_3$ and other $Sr_{1+x}TiS_3$, however, distort the TiS_6 chains in incommensurate manner, periodically introducing rotational distortion to TiS_6 polyhedron.[26] The presence of localized Ti *d*-states, commensurate with the excess Sr, significantly increases the birefringence of $Sr_{9/8}TiS_3$ to a much higher region, up to 2.1.[26]

6. Conclusion

In this article, we demonstrated another member of the quasi-1D perovskite chalcogenide $A_{1+x}TiX_3$ (A = Sr, Ba; X = S, Se), $BaTiSe_3$, to be highly optically anisotropic at room temperature. We synthesized and studied the single crystals of $BaTiSe_3$, formerly reported[30] as $P6_3/mmc$ space group in powder form. The high-quality $BaTiSe_3$ crystals adopt antiparallel displacements and off-centric octahedra symmetry breaking along the *c*-axis whose periodicity follows a $2\sqrt{3}\times2\sqrt{3}\times1$ supercell with *P*31*c* symmetry. Despite the long-range structural complexity from a larger supercell compared to $BaTiS_3$, $BaTiSe_3$ crystals possess an analogous uniaxial optical axis parallel to the long axis of the needle, with giant birefringence (Δn up to 0.9) in a broadband spectral region across the MWIR and LWIR ranges. We anticipate the class of quasi-1D chalcogenides, ABX_3 (A = Sr, Ba, ..., B = Ti, Zr, ..., and X = S, Se, ...) to cover a wide spectral range of optical and optoelectronic anisotropy, leading to miniaturized polarization resolved IR devices for sensing and telecommunications.

7. Experimental Section

Crystal Growth: Single crystals of $BaTiSe_3$ were grown by chemical vapor transport with iodine as a transporting agent. Stoichiometric amounts of barium selenide, titanium, and selenium precursors were mixed with iodine in a nitrogen-filled glovebox before being loaded in a quartz ampule. The quartz tube was then evacuated and sealed with a blowtorch. The sealed ampoule was heated to the reaction temperature of 945 °C at

100 °C per hour and dwelled for 100 h before being cooled down within the tube furnace. More details in Section S1 (Supporting Information).

X-Ray Diffraction: XRD studies were performed in a Bruker D8 Advance X-ray diffractometer in parallel beam configuration, using a germanium (004) two-bounce monochromator for Cu $K\alpha 1$ ($\lambda = 1.5406$ Å) radiation. Crystals were loaded on the Compact Cradle on top of a glass-slide holder. Diffractions were carried out in the out-of-plane mode while sweeping the χ-tilting. The rocking curve was measured for the strongest 200 reflections.

Single-Crystal X-Ray Diffraction: Synchrotron single-crystal X-ray diffractions were carried out at beamline 12.2.1 at the Advanced Light Source (ALS), Lawrence Berkeley National Laboratory; and beamline 15-ID-B at the Advanced Photon Source, Argonne National Laboratory. More details are reported in Table S1 (Supporting Information). Crystals were submerged in oil and cut to the preferred sizes before mounted to the MiTeGen Kapton loops for SC-XRD. Despite being held at room temperature, the nitrogen cryostream was left on to provide an inert atmosphere to avoid progressive surface degradation of $BaTiSe_3$ potentially via oxidation throughout the measurements.

Crystal structures were pre-determined by the Rigaku XtaLAB diffractometer at the University of Southern California. The diffractometer was equipped with a Rigaku (Mo Kα) rotating-anode X-ray tube and a hybrid pixel array detector. Diffraction data were collected using a wavelength of 0.71073 Å.

At ALS 12.2.1, the crystal was placed on the goniometer head of a Bruker D8 diffractometer, which is equipped with a PHOTON100 CMOS detector operating in shutter-less mode. Diffraction data were collected using synchrotron radiation monochromate with a wavelength of 0.72880 Å with silicon (111).

At APS 15-ID-B, the crystal was placed on the goniometer head of a Bruker D8 diffractometer, which is equipped with a Pilatus 3 × 2 M detector operating in shutter-less mode. Diffraction and mask data were collected using synchrotron radiation monochromate with a wavelength of 0.41328 Å with silicon (111).

Unit cell determination, integration, and scaling were then carried out in Bruker APEX 3. The precession map was integrated up to a resolution of 1.5 Å with a thickness of 0.1. Crystal structure determination and refinement were done in ShelXle,[33] where an electron density map was also extracted.[44] All possible space groups and pseudo-merohedral twins were tested to find the best matching crystal structure.

Scanning Transmission Electron Microscopy: The cross sectional STEM sample of the $BaTiSe_3$ crystal was prepared using a Thermo Scientific Helios G4 PFIB UXe Dual Beam system. Standard in situ lift-out was employed during the preparation of the TEM lamella. The sample surface was protected from ion-beam damage by depositing carbon and tungsten protective layers. The TEM lamella was first milled to ≈160 nm with a 10 pA beam current from a 30 kV ion beam, followed by gentler milling at 5 kV to a thickness of ≈60 nm. A subsequent lowering of the ion beam energy to 2 kV minimizes the surface damage of the lamella.

HAADF-STEM images were recorded using a probe-corrected Thermo Fisher Scientific Spectra 200 scanning transmission electron microscope operated at 200 kV, equipped with a fifth-order aberration corrector and an X-CFEG cold field emission electron gun. The $BaTiSe_3$ crystal was tilted along the [001] zone axis for image acquisition. The STEM images were acquired using a probe with a semi-convergence angle of 25 mrad and a current of 90 pA, with the inner and outer collection angles of the ADF detector at 53 and 200 mrad, respectively. For each acquisition, multiple frames (over 40) were captured with a pixel dwell time of 200 ns, followed by rigid registration and averaging to improve the signal-to-noise ratio. The atomic positions were precisely determined with aid from the center of mass refinement and 2-D Gaussian fitting using Atomap.[45] Image analysis was performed with a custom Python script. The displacements of the titanium and selenium atoms were calculated concerning the barium hexagons.

Raman Spectroscopy: Polarization-resolved Raman spectroscopy was performed in a backscattering geometry using a confocal microscope spectrometer (Horiba Evolution). The incident beam (532 nm) was focused on a 1–2 µm size spot with a 50× objective lens. Laser power was set to ≈100 µW. The integration time of the spectrometer was 10 min. The beam was linearly polarized, and a half-wave plate was placed before the objective for polarization rotation. The analyzer was placed in front of the spectrometer entrance and was set parallel/perpendicular to the incident polarization when measuring XX or XY channels respectively. During polarization dependence scans, the half-wave plate was rotated from 0° to 180° with a 7.5° step. Space (point) groups were compared between $P6_3/mmc$ (D_{6h}) and $P31c$ (C_{3v}), details in the Supporting Information.

Fourier Transform Infrared Spectroscopy (FTIR): Infrared spectroscopy was performed using a Fourier-transform infrared spectrometer (Bruker Vertex 70) connected to an infrared microscope (Hyperion 2000). A 15× Cassegrain microscope objective (numerical aperture = 0.4) was used for both transmission and reflection measurements at near-normal incidence. A KRS-5 wire grid polarizer controls the polarization of the incident beam for 2–30 µm. FTIR measurements were performed with a Globar source, a potassium bromide beam splitter, and a mercury-cadmium-telluride (MCT) detector.

$BaTiSe_3$ crystals were suspended from the edge of a Si handle wafer using Kapton tape. The pre-determined crystal orientation was manually matched with the polarizer orientation. Transmittance and reflectance spectra were collected at 0° and 90° rotation from the *a*-axis.

Spectroscopic Ellipsometry: Variable-angle spectroscopic ellipsometry measurements were performed using a VASE ellipsometer with focusing probes (J. A. Woollam Co.) over a spectral range of 210 to 2500 nm at an angle of incidence of 55°. Data were acquired from four different sample orientations (optical axis perpendicular, parallel, 30°, and 18° to the plane of incidence). Data analysis and refractive index extraction were performed using WVASE software,[46] (J. A. Woollam Co.). More details can be found in Section S7 (Supporting Information).

First-Principles Calculations: Performed within the framework of density functional theory, implemented in the OpenMX package.[47] The pseudoatomic orbitals,[48] were generated with the cutoff radius of 10, 7.0, and 7.0 a. u., for Ba, Ti, and Se elements, and basis sets of *s3p2d2*, *s3p2d1*, and *s3p2d2*[49] for these three elements,[50] which had been tested well enough to describe the system. The exchange-correlation energy functional was adopted, which was parameterized by Perdew, Burke, and Ernzerhof (PBE),[51] within the generalized gradient approximation. Internal atomic positions were relaxed starting from the experimental lattice constants. The energy cutoff was set to 160 Ry, and the energy convergence criterion of self-consistent calculations was 10^{-6} Hartree. Internal atomic positions were relaxed starting from the experimental lattice constants, with the force convergence of 10^{-3} Hartree/bohr. Spin-orbit coupling was included self-consistently through the *j*-dependent pseudopotential, with the Γ-centered *k*-mesh grid of 5 × 5 × 9.

Supporting Information

Supporting Information is available from the Wiley Online Library or from the author.

Acknowledgements

The authors appreciate the guidance from Dr. Gwan-Yeong Jung, and Prof. Rohan Mishra from the Washington University at St. Louis; and Dr. Jiangbin Wu from the Chinese Academy of Sciences. This work was supported by the Army Research Office (ARO) MURI program with award number W911NF-21-1-0327 and the US National Science Foundation with award number DMR-2122071. The crystal growth capabilities were in part supported by an ONR grant with award number N00014-23-1-2818. H.M. and M.K. acknowledge the support from the Office of Naval Research (N00014-20-1-2297). The preliminary crystal structure is screened by the single crystal diffraction instrumentation supported by National Science Foundation award number CHE-2018740 and by the Raman spectroscopy supported by the U.S. Department of Energy, Office of Basic Energy Sciences under Award No. DE-FG02-0746376. This research used resources from the Advanced Light Source, which is a DOE Office of Science User Facility

under contract no. DE-AC02-05CH11231; and the NSF's ChemMatCARS Sector 15 at the Advanced Photon Source (APS), Argonne National Laboratory (ANL), which is supported by the Divisions of Chemistry (CHE) and Materials Research (DMR), National Science Foundation, under grant number NSF/CHE- 1834750. The authors gratefully acknowledge the use of facilities and instrumentation at the UW-Madison Wisconsin Centers for Nanoscale Technology (wcnt.wisc.edu) partially supported by the NSF through the University of Wisconsin Materials Research Science and Engineering Center (DMR-1720415). B.I. and N.G. were supported by the US Department of Energy, BES DMSE, and the Gordon and Betty Moore Foundation's EPiQS Initiative Grant GBMF9459. Q.S. and R.C. were supported by the National Science Foundation under Grant No. 1751739. T.R.L. and Y.T.S. acknowledge support from the USC Viterbi startup funding, Taiwan-USC scholarship, and the USC Research and Innovation Instrumentation Award. Electron microscopy data were acquired at the Core Center of Excellence in Nano Imaging at the University of Southern California. B.Z. acknowledges technical support from Mythili Surendran and Harish Kumarasubramanian.

Conflict of Interest

The authors declare no conflict of interest.

Data Availability Statement

The data that support the findings of this study are available from the corresponding author upon reasonable request.

Keywords

optical anisotropy, quasi-1D chalcogenide, Raman spectroscopy, single crystals, X-ray diffraction

Received: February 3, 2024
Revised: July 19, 2024
Published online: September 3, 2024

[1] Q. Weng, *ISPRS J. Photogramm. Remote Sens.* **2009**, *64*, 335.
[2] B. S. Robinson, D. M. Boroson, C. M. Schieler, F. I. Khatri, O. Guldner, S. Constantine, T. Shih, J. W. Burnside, F. Q. Hakimi, B. C. Bilyeu, A. Garg, G. Allen, E. Clements, D. M. Cornwell, in *Free-Space Laser Communication and Atmospheric Propagation XXX* (Eds: H. Hemmati, D. M. Boroson), SPIE, San Francisco, USA **2018**, p. 31.
[3] M. Grgic, K. Delac, S. Grgic, *Multimedia Tools Appl.* **2011**, *51*, 863.
[4] K.-N. Liou, *An Introduction to Atmospheric Radiation*, Academic Press, Amsterdam, Boston **2002**.
[5] W. Minkina, S. Dudzik, *Infrared Thermography: Errors and Uncertainties*, Wiley, Hoboken, NJ **2009**.
[6] I. Adjabi, A. Ouahabi, A. Benzaoui, A. Taleb-Ahmed, *Electronics* **2020**, *9*, 1188.
[7] D. L. Hickman, M. I. Smith, K. S. Kim, H.-J. Choi, presented at Automatic Target Recognition XXVII, Anaheim, California, USA, May **2017**.
[8] C. Yonezawa, M. Watanabe, G. Saito, *Remote Sens.* **2012**, *4*, 2314.
[9] A. Chael, A. Lupsasca, G. N. Wong, E. Quataert, *Astrophys. J.* **2023**, *958*, 65.
[10] B. Laude-Boulesteix, A. De Martino, B. Drévillon, L. Schwartz, *Appl. Opt.* **2004**, *43*, 2824.
[11] N. A. Rubin, G. D'Aversa, P. Chevalier, Z. Shi, W. T. Chen, F. Capasso, *Science* **2019**, *365*, aax1839.
[12] F. Yang, K. Li, M. Fan, W. Yao, L. Fu, C. Xiong, S. Jiang, D. Li, M. Xu, C. Chen, G. Zhang, J. Tang, *Adv. Opt. Mater.* **2022**, *11*, 2201859.
[13] S. Wu, Y. Chen, X. Wang, H. Jiao, Q. Zhao, X. Huang, X. Tai, Y. Zhou, H. Chen, X. Wang, S. Huang, H. Yan, T. Lin, H. Shen, W. Hu, X. Meng, J. Chu, J. Wang, *Nat. Commun.* **2022**, *13*, 3198.
[14] W. M. Sinton, *J. Opt. Soc. Am.* **1961**, *51*, 1309.
[15] G. Ghosh, *Opt. Commun.* **1999**, *163*, 95.
[16] D. E. Zelmon, D. L. Small, D. Jundt, *J. Opt. Soc. Am. B* **1997**, *14*, 3319.
[17] H. T. Luo, T. Tkaczyk, E. L. Dereniak, K. Oka, R. Sampson, *Opt. Lett.* **2006**, *31*, 616.
[18] Q. Xu, Y. Liu, Q. Wu, L. Hou, Y. Li, L. Li, Z. Lin, S. Zhao, J. Luo, *Sci. China Mater.* **2023**, *66*, 3271.
[19] C. Jin, F. Li, B. Cheng, H. Qiu, Z. Yang, S. Pan, M. Mutailipu, *Angew. Chem., Int. Ed.* **2022**, *61*, 202203984.
[20] S. Krimm, *Infrared Spectra of High Polymers. In: Fortschritte Der Hochpolymeren-Forschung*, Springer-Verlag, Berlin/Heidelberg **1960**, pp. 51–172.
[21] S. Niu, G. Joe, H. Zhao, Y. Zhou, T. Orvis, H. Huyan, J. Salman, K. Mahalingam, B. Urwin, J. Wu, Y. Liu, T. E. Tiwald, S. B. Cronin, B. M. Howe, M. Mecklenburg, R. Haiges, D. J. Singh, H. Wang, M. A. Kats, J. Ravichandran, *Nat. Photonics* **2018**, *12*, 392.
[22] S. Niu, H. Zhao, Y. Zhou, H. Huyan, B. Zhao, J. Wu, S. B. Cronin, H. Wang, J. Ravichandran, *Chem. Mater.* **2018**, *30*, 4897.
[23] B. Zhao, M. S. B. Hoque, G. Y. Jung, H. Mei, S. Singh, G. Ren, M. Milich, Q. Zhao, N. Wang, H. Chen, S. Niu, S.-J. Lee, C.-T. Kuo, J.-S. Lee, J. A. Tomko, H. Wang, M. A. Kats, R. Mishra, P. E. Hopkins, J. Ravichandran, *Chem. Mater.* **2022**, *34*, 5680.
[24] H. Chen, A. Avishai, M. Surendran, J. Ravichandran, *ACS Appl. Electron. Mater.* **2022**, *4*, 5550.
[25] B. Sun, S. Niu, R. P. Hermann, J. Moon, N. Shulumba, K. Page, B. Zhao, A. S. Thind, K. Mahalingam, J. Milam-Guerrero, R. Haiges, M. Mecklenburg, B. C. Melot, Y.-D. Jho, B. M. Howe, R. Mishra, A. Alatas, B. Winn, M. E. Manley, J. Ravichandran, A. J. Minnich, *Nat. Commun.* **2020**, *11*, 6039.
[26] H. Mei, G. Ren, B. Zhao, J. Salman, G. Y. Jung, H. Chen, S. Singh, A. S. Thind, J. Cavin, J. A. Hachtel, M. Chi, S. Niu, G. Joe, C. Wan, N. Settineri, S. J. Teat, B. C. Chakoumakos, J. Ravichandran, R. Mishra, M. A. Kats, *Adv. Mater.* **2023**, *35*, 2303588.
[27] B. Zhao, G. Ren, H. Mei, V. C. Wu, S. Singh, G. Jung, H. Chen, R. Giovine, S. Niu, A. S. Thind, J. Salman, N. S. Settineri, B. C. Chakoumakos, M. E. Manley, R. P. Hermann, A. R. Lupini, M. Chi, J. A. Hachtel, A. Simonov, S. J. Teat, R. J. Clément, M. A. Kats, J. Ravichandr, R. Mishra, *Adv. Mater.* **2024**, *36*, 2311559.
[28] S. A. Kulkarni, T. Baikie, P. P. Boix, N. Yantara, N. Mathews, S. Mhaisalkar, *J. Mater. Chem. A* **2014**, *2*, 9221.
[29] C.-Z. Ning, L. Dou, P. Yang, *Nat. Rev. Mater.* **2017**, *2*, 17070.
[30] L. A. Aslanov, *Russ. J. Inorg. Chem.* **1964**, *9*, 1090.
[31] H. Chen, B. Zhao, J. Mutch, G. Y. Jung, G. Ren, S. Shabani, E. Seewald, S. Niu, J. Wu, N. Wang, M. Surendran, S. Singh, J. Luo, S. Ohtomo, G. Goh, B. C. Chakoumakos, S. J. Teat, B. Melot, H. Wang, J. Ravichandran, *Adv. Mater.* **2023**, *35*, https://doi.org/10.1002/adma.202303283.
[32] Y. Waseda, E. Matsubara, K. Shinoda, *X-Ray Diffraction Crystallography: Introduction, Examples and Solved Problems*, Springer, Heidelberg, Germany **2011**.
[33] G. M. Sheldrick, *Acta Crystallogr., C Struct. Chem.* **2015**, *71*, 3.
[34] N. B. Colthup, L. H. Daly, S. E. Wiberley, *Introduction to Infrared and Raman Spectroscopy*, Academic Press, Boston, **1990**.
[35] J. Wu, X. Cong, S. Niu, F. Liu, H. Zhao, Z. Du, J. Ravichandran, P. Tan, H. Wang, *Adv. Mater.* **2019**, *31*, 1902118.
[36] M. I. Aroyo, J. M. Perez-Mato, D. Orobengoa, E. Tasci, *Bulg. Chem. Commun.* **2011**, *43*, 183.
[37] N. Ismail, C. C. Kores, D. Geskus, M. Pollnau, *Opt. Express* **2016**, *24*, 16366.

[38] J. Chamberlain, J. E. Gibbs, H. A. Gebbie, *Infrared Phys.* **1969**, *9*, 185.
[39] A. Segura, L. Artús, R. Cuscó, T. Taniguchi, G. Cassabois, B. Gil, *Phys. Rev. Mater.* **2018**, *2*, 024001.
[40] Z. Guoqing, X. Jun, C. Xingda, Z. Heyu, W. Siting, X. Ke, D. Peizhen, G. Fuxi, *J. Cryst. Growth* **1998**, *191*, 517.
[41] D. B. Chenault, R. A. Chipman, *Appl. Opt.* **1993**, *32*, 4223.
[42] M. J. Dodge, *Appl. Opt.* **1984**, *23*, 1980.
[43] D. N. Nikogosian, *Nonlinear Optical Crystals: A Complete Survey*, Springer-Science, New York **2005**.
[44] C. B. Hübschle, G. M. Sheldrick, B. Dittrich, *J. Appl. Crystallogr.* **2011**, *44*, 1281.
[45] M. Nord, P. E. Vullum, I. MacLaren, T. Tybell, R. Holmestad, *Adv. Struct. Chem. Imaging* **2017**, *3*, 9.
[46] J. Woollam, JA Woollam Company, Lincoln, NE, USA **2012**.
[47] OpenMX website, https://www.openmx-square.org/, (accessed: July 2024).
[48] T. Ozaki, H. Kino, *Phys. Rev. B* **2005**, *72*, 045121.
[49] Optimized basis functions provided by the database Ver, https://www.openmx-square.org/openmx_man3.9/node27.html, (accessed: July 2024).
[50] T. Ozaki, H. Kino, *Phys. Rev. B* **2004**, *69*, 195113.
[51] J. P. Perdew, K. Burke, M. Ernzerhof, *Phys. Rev. Lett.* **1996**, *77*, 3865.